Astronomy & Astrophysics

DOT tomography of the solar atmosphere

III. Observations and simulations of reversed granulation

J. Leenaarts[1] and S. Wedemeyer-Böhm[2]

[1] Sterrekundig Instituut, Utrecht University, Postbus 80 000, 3508 TA Utrecht, The Netherlands
    e-mail: j.leenaarts@astro.uu.nl
[2] Kiepenheuer-Institut für Sonnenphysik, Schöneckstrasse 6, 79104 Freiburg, Germany
    e-mail: wedemeyer@kis.uni-freiburg.de

Abstract. We compare high-quality image sequences from the Dutch Open Telescope (DOT) with synthetic image sequences obtained from 3D radiation-hydrodynamics simulations of the solar granulation. In particular, we study the subsonic brightness pattern observed in the wings of Ca II H & K. The simulations reproduce the observed intensity contrast, time scales, and Fourier behaviour rather well. Most differences can be attributed to the resolution difference between the observations and the simulation and the small geometrical extent of the simulation. We conclude that magnetic fields play no major role in the formation of reversed granulation.

Key words. Sun: photosphere – Sun: chromosphere – Sun: magnetic fields

1. Introduction

Intensity maps of quiet-sun internetwork areas taken in the wings of the Ca II H & K lines show a pattern of dark cells with bright inter-cellular boundaries. It resembles the granulation pattern, but with the brightness reversed. This pattern is commonly referred to as "reversed granulation" (see, e.g., Evans & Catalano 1972; Suemoto et al. 1987, 1990 and further references in Rutten & Krijger 2003) and originates from a layer a few hundred kilometers above the granulation. In this paper we present a detailed comparison between observations of reversed granulation and synthetic intensity maps obtained from hydrodynamical simulations of the non-magnetic solar atmosphere. Recent observations of reversed granulation were reported in the second paper of this series by (Rutten et al. 2004a, henceforth Paper II) who suggest that reversed granulation is a mixture of convection reversal and internal gravity waves. They conclude that comparison between observations and numerical simulations is needed to verify this suggestion. We perform such a comparison in this paper.

We use both the observations reported in Paper II and newer observations obtained with the Dutch Open Telescope (DOT). Synthetic intensity maps were obtained from the numerical simulations of Wedemeyer et al. (2004) combined with the SPANSAT radiative transfer code of V.A. Sheminova (Gadun & Sheminova 1988). In this paper we apply the diagnostics employed in Paper II to these synthetic intensity maps.

In Sect. 2 we present the new observations. The production of the synthetic intensity maps is described in Sect. 3. In Sect. 4 we present a comparison between the observations and the simulations. We end with discussion and conclusions in Sect. 5. We reproduce Figs. 4–7 of Paper II here for convenience.

2. Observations

Two datasets are used in this paper. The first, obtained with the DOT on December 8, 2002, is described in detail in Paper II. The second set was obtained with the DOT during UT 07:40–09:15 on June 18, 2003.

It consists of multiple 14-min sequences taken at a cadence of 25 s per speckle burst covering the solar center-to-limb variation synchronously in four passbands: red continuum (6540 Å), blue continuum (4320 Å), Ca II H (3968 Å), and G band (4305 Å). The Ca II H sequence is a dual one, made by sequentially switching the filter passband from line center (3968.83 Å, filter *FWHM* 1.285 Å) to a location in the inner wing (3966.67 Å, *FWHM* filter 1.758 Å) between successive bursts. The image sequences were dark-subtracted, flat-fielded and speckle-reconstructed using the standard DOT data reduction procedures described in Rutten et al. (2004b) and Paper II. In the present paper we use only the blue continuum, G band, and Ca II H filtergrams from the $\mu = 0.98$ sequence. During this sequence the seeing was fair, with the Fried parameter ranging from $r_0 = 5.8$ cm to $r_0 = 10.6$ cm.

3. Simulations

A time series of synthetic intensity maps was computed from numerical simulations obtained with the CO^{5}BOLD 3D radiation hydrodynamics code developed by Freytag & Steffen and described in Freytag et al. (2002), Wedemeyer et al. (2004), and in more detail in Wedemeyer (2003). The hydrodynamics part uses operator splitting and a fast approximate Riemann solver, and has a small amount of tensor viscosity added to increase numerical stability. Radiation transport is solved in LTE using long characteristics in the grey approximation. The Rosseland mean opacities are based on OPAL (Iglesias et al. 1992) and PHOENIX (Hauschildt et al. 1997) data. The simulation box consists of $140 \times 140 \times 200$ grid cells with horizontal resolution 40 km and extent 5600 km $\times$ 5600 km. The vertical extent ranges from -1400 to $+1710$ km with the origin of the height axis ($z = 0$ km) at average Rosseland optical depth unity. The vertical resolution is height-dependent, varying from a grid spacing of 46 km at the bottom of the box to 12 km above $z = -270$ km, The lower boundary is open, allowing material to flow in and out of the box, while the boundary at the top is transmitting and thus does not hinder waves and shocks from leaving the box. The lateral boundary conditions are periodic.

For the present paper we selected output from the simulation consisting of data cubes describing the physical state of the atmosphere (temperature, density, velocity, etc.) in 116 time steps at 30 s cadence. From these we computed Ca II H wing intensity maps at $\mu = 1$ assuming LTE. This assumption simplifies the radiative transfer to straightforward 1D LTE evaluation along each vertical column. We used the SPANSAT radiative transfer code of V.A. Sheminova (cf. Gadun & Sheminova 1988), including collisional line broadening by neutral hydrogen following the Barklem recipe (Barklem & O'Mara 1998).

We calculated intensity maps for different wavelengths in the blue wing of the Ca II H line, ranging from 3960.0 Å to 3967.8 Å with an increment of 0.2 Å. The blends in the Ca II H wing were neglected because a test showed that their inclusion has only a minor effect on the resulting synthetic images. For the contrast comparison of Sect. 4 below we multiplied the synthetic spectra with the DOT Ca filter transmission profile of the June 2003 data. Throughout the paper we use the 3960 Å continuum image sequence as a proxy for the observed blue continuum and the G band, and refer to this as synthetic blue continuum. The exact wavelength position of the Ca II H bandpass in the December 2002 data is not known. By comparing the synthetic images with the observations we judged 3967.4 Å to be a representative wavelength for the December 2002 Ca II H data.

We compared the results of the SPANSAT calculations with calculations done with the LINFOR3D radiative transfer code (http://www.aip.de/~mst/linfor3D_main.html). Both calculations yielded in general identical results.

Sample images of the simulated blue continuum and Ca II H are shown in the top row of Fig. 1. The time lag between the two wavelengths is chosen in agreement with the result in Fig. 3. Inspection of the simulation shows that 80% of the emergent intensity at 3967.4 Å originates between 200 km and 600 km height, with an average formation height of 350 km.
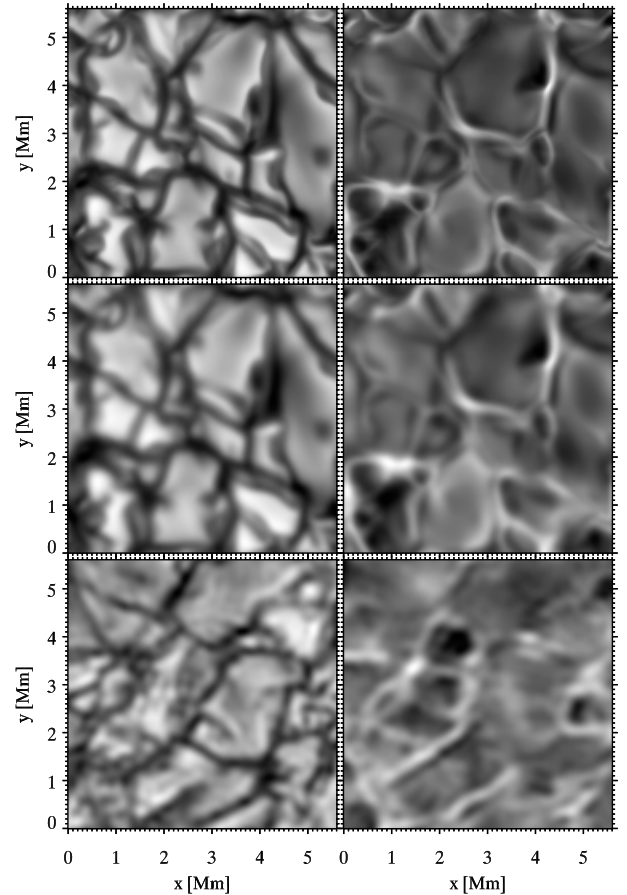

Fig. 1. Simulated and observed images of the blue continuum (left-hand column) and Ca II H wing (right-hand column). The time lag between blue continuum and Ca II H is 120 s for the simulated image pairs and 150 s for the observed pair. *Top row*: simulation data. *Middle row*: simulation data convolved with the best-fit telescope point spread function. *Bottom row*: observations of June 18, 2003. The graininess of the observations is due to camera noise.

4. Analysis and results

Contrast comparison. It is difficult to correctly mimic the image degradation by the telescope and the earth's atmosphere. One may measure this degradation utilizing a partial solar eclipse (Levy 1971; Deubner & Mattig 1975; Nordlund 1984a), but this has not been done for the DOT. We therefore try to estimate a point spread function with the procedure of Schüssler et al. (2003). It assumes that the core of the point spread function is an Airy function corresponding to the DOT aperture of 45 cm. A Lorentz function is added to describe the effects of atmospheric motion, dust on the optics, and other imperfections. The Lorentzian is defined by two parameters, α, its height relative to the height of the Airy core and β, the *FWHM* of the wings. Unfortunately, analysis shows that there is a wide range of (α, β) combinations that fit the observations rather well. Eventually, we chose $\alpha = 0.014$ and $\beta = 400$ km as best-fit values, but note that similar results are produced with other combinations.

In the right-hand panels of Fig. 2 we compare the brightness contrast profiles from the June 2003 observations with their synthetic counterparts obtained through convolution with the
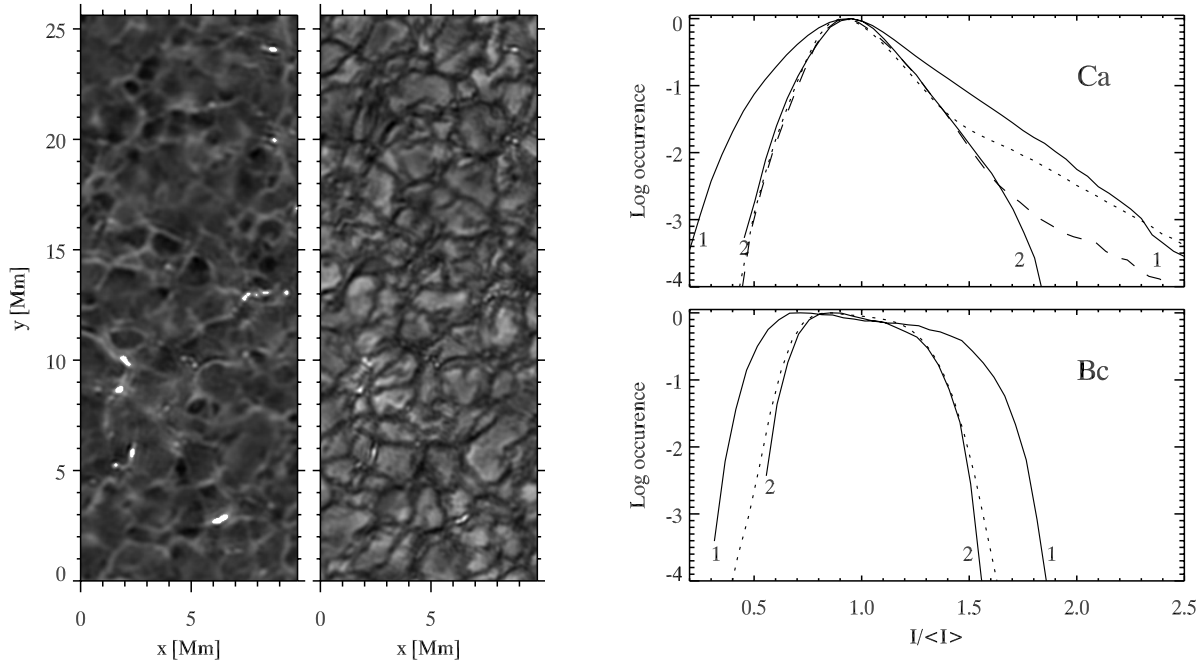
Fig. 2. Left-hand panels: Ca II H (*left*) and G-band (*right*) brightness images from the June 18, 2003 observations. The filled white contours in the Ca II H image denote areas with $I/\langle I\rangle \geq 1.8$. Right-hand panels: normalized occurrence distributions of the intensity divided by the spatial and temporal mean. Lower-right panel: blue continuum. Upper-right panel: Ca II H wing. The solid curves are simulation data smeared with a point spread function with $\alpha = 0.014$ and $\beta = 0$ km (1) and 400 km (2). The dotted curves are observations from June 18, 2003. The dashed curve in the upper panel is the occurrence distribution for the quiet subfield of the June 18 observations shown in the left-hand panels.

adopted point spread function. Smearing with the Airy function alone does not fit the observations (curve 1). Our choice of α and β fits both the blue continuum contrast and the Ca II H contrast rather well (curve 2), except for the high-contrast tail in the Ca II H observations. We attribute the latter to the presence of magnetic fields in the data because the intensity contrast distribution of the quiet subfield shows a lower high-contrast tail than the curve for the whole field, and because the image pair in the left-hand panels of Fig. 2 shows that most if not all of the residual high-contrast pixels in Ca II H are co-spatial with bright points in the G band, and are therefore likely to represent magnetic elements.

Concerning the simulations, it should be pointed out that the grey approximation overestimates the temperature contrast in layers above the middle photosphere (Vögler 2004, Fig. 3; Wedemeyer 2003, Fig. 8.2). In addition, our synthetic blue continuum images show slightly higher contrast than the observed continuum at 4300 Å because of the larger temperature sensitivity of the Planck function at shorter wavelengths. Despite these deficiencies, the good quality of the fit in Fig. 2 at both wavelengths simultaneously gives confidence that the simulation reproduces the actual contrast quite well.

Time-delay correlations. In order to study the pattern evolution of the reversed granulation, and following Paper II, we low-pass filtered the synthetic blue continuum and Ca II H sequences to remove all components with apparent supersonic horizontal speed. This was done by Fourier transforming the cube, setting all Fourier components with

$\omega\,(k_x^2 + k_y^2)^{-0.5} > 7$ km s^{-1} equal to zero and transforming back to the (x, y, t) domain.

Figure 3 compares results presented in Fig. 4 of Paper II with their synthetic counterpart. The curves represent temporal auto- and cross-correlation functions per pixel, averaged over many pixels after the low-pass filtering. As in Paper II, we limited the averaging to the internetwork pixels for the observations but used all pixels of the simulations because they contain no magnetic fields. The correlation curves are an indicator for the timescale at which patterns in the image sequences evolve.

In the upper panel the autocorrelation curves for the simulations and the internetwork observations are presented. The $1/e$ time for the simulated blue continuum is 5.1 min as compared to 4.5 min for the G band observations. The curves agree very well for the first 4 minutes, but the simulated blue continuum has a higher correlation at longer delays than the observed G band. The $1/e$ time for the simulated Ca II H is 1.5 min as compared to 3.0 min for the observed Ca II H.

We attribute this difference to the selection of the internetwork in Paper II. Inspection showed that it still contained small bright persistent features that are likely to represent isolated magnetic elements (Brandt et al. 1992, 1994). We therefore selected a much smaller pixel subset which does not contain any such obvious or suspected magnetic element. The autocorrelation for this more selective sample is also plotted in Fig. 3. It has an $1/e$ time of only 2.0 min, which suggests that the apparent discrepancy between the dotted and solid Ca curves in the upper panel of Fig. 3 is due to magnetism. We attribute the remaining difference to lack of spatial resolution, because smoothing the simulated Ca II H images to 0.5 arcsec
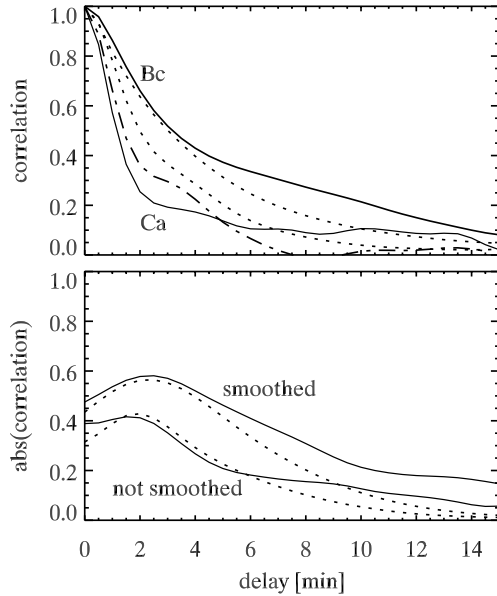
Fig. 3. Temporal evolution of pattern correlations in the December 8, 2002 observations and the simulations, restricted to subsonic changes. *Upper panel*: autocorrelation for synthetic blue continuum (upper solid curve) and Ca (lower solid curve), and observed internetwork G band (upper dotted curve) and Ca (lower dotted curve). Dash-dotted curve: observed Ca autocorrelation for nonmagnetic areas. *Lower panel*: sign-reversed cross-correlations between synthetic blue continuum and Ca II H (solid) and between observed G band and Ca II H (dotted). The upper curves result when the images are spatially smoothed to 1.5 arcsec resolution.

resolution (the effective resolution of the December 8, 2002 data) increases the Ca-Ca autocorrelation $1/e$ time to 1.9 min. We evaluated the other correlations (Bc–Bc and Bc–Ca) also for our more stringent sample and compared these with the results in Fig. 4 of Paper II but found no significant differences.

Fourier representations. Figures 4–6 contain the Fourier analysis of the simulations and the 2002 observations. The simulation panels are obtained from the synthetic blue continuum and 3967.4 Å image sequences convolved with the best-fit point spread function. The upper panel of Fig. 4 shows modulation phase differences $\Delta\phi$ (Bc – Ca). The simulations agree reasonably well with the observations. The simulation plot is noisier because of the smaller number of pixels in the spatial directions. The power spectra in the lower panel agree well with the observations. The main difference is the double-peaked increase in Ca power around 4 mHz as opposed to the smooth peak in the observations. This is due to the limited vertical size of the simulation box, causing the vertical oscillation eigenfrequencies of the box to be more broadly spaced than on the Sun (Leibacher et al. 1982; Stein & Nordlund 2001).

Figure 5 shows a decomposition of blue continuum and Ca II H brightness power into temporal and spatial frequencies. The resolution in spatial frequency of the simulations is much lower than in the observations because of the smaller horizontal size of the computational box. Owing to the absence of magnetic fields in the simulation there is less power at the largest scales and lowest frequencies in the simulation. The
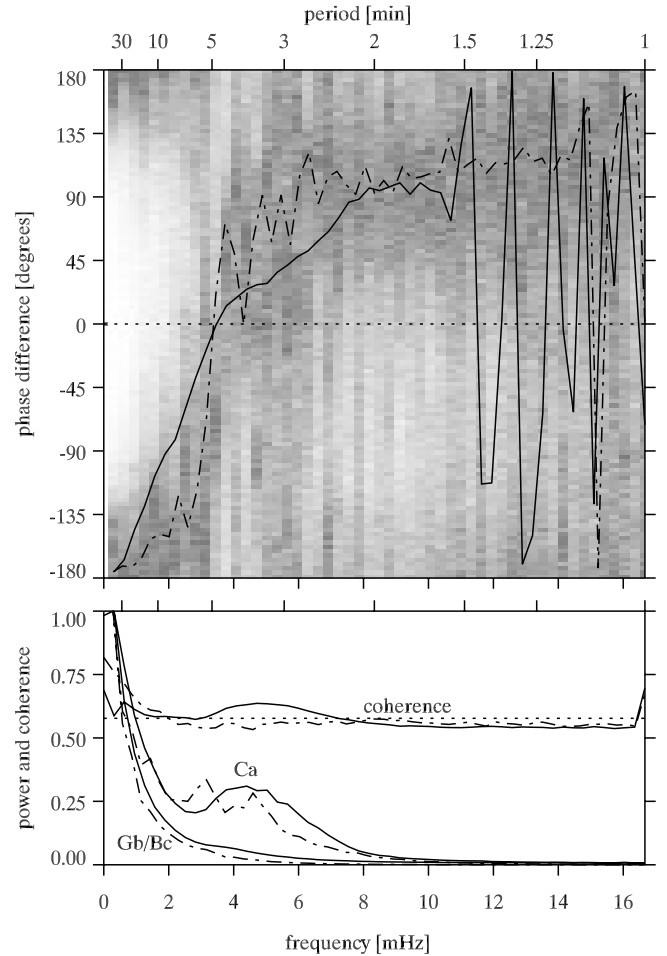

Fig. 4. Fourier spectra for observed G band and Ca II H (solid) and simulated blue continuum and Ca II H (dash-dotted). *Upper panel*: phase differences $\Delta\phi$ (Bc/Gb – Ca) between blue continuum / G band and Ca II H brightness. Grey scale: amplitude-weighted phase differences per pixel following the recipe of Krijger et al. (2001) for the simulations. The jagged fluctuations of the mean curve of the observations above $f = 10$ mHz indicate domination by noise. The lower panel shows the corresponding power spectra, mean and trend removed, normalized at the first non-zero frequency, and coherence spectra with dotted noise estimate.

low-frequency power seems to extend to larger wavenumber in the synthetic blue continuum than in the observed G band. Also notice the increased power along the f-mode ridge in the synthetic blue continuum panel and the two discrete patches of power at 3 and 5 mHz at zero wavenumber in the synthetic Ca II H panel caused by vertical eigenmodes.

The upper panels of Fig. 6 show phase differences $\Delta\phi$ (Bc/Gb–Ca). Contrary to Fig. 7 in Paper II, we do not plot contours but the raw pixels. The simulations show reversed granulation as a patch of negative phase difference below the Lamb line, comparable to the observations but extending to $k_h \approx 8$ arcsec^{-1} instead of $k_h \approx 5$ arcsec^{-1}. The extended p-mode patch of positive phase difference above the Lamb line in the observations is not present in the simulations, although the simulations show a patch of positive phase slightly below the Lamb line ranging over $k_h = 4-12$ arcsec^{-1}.
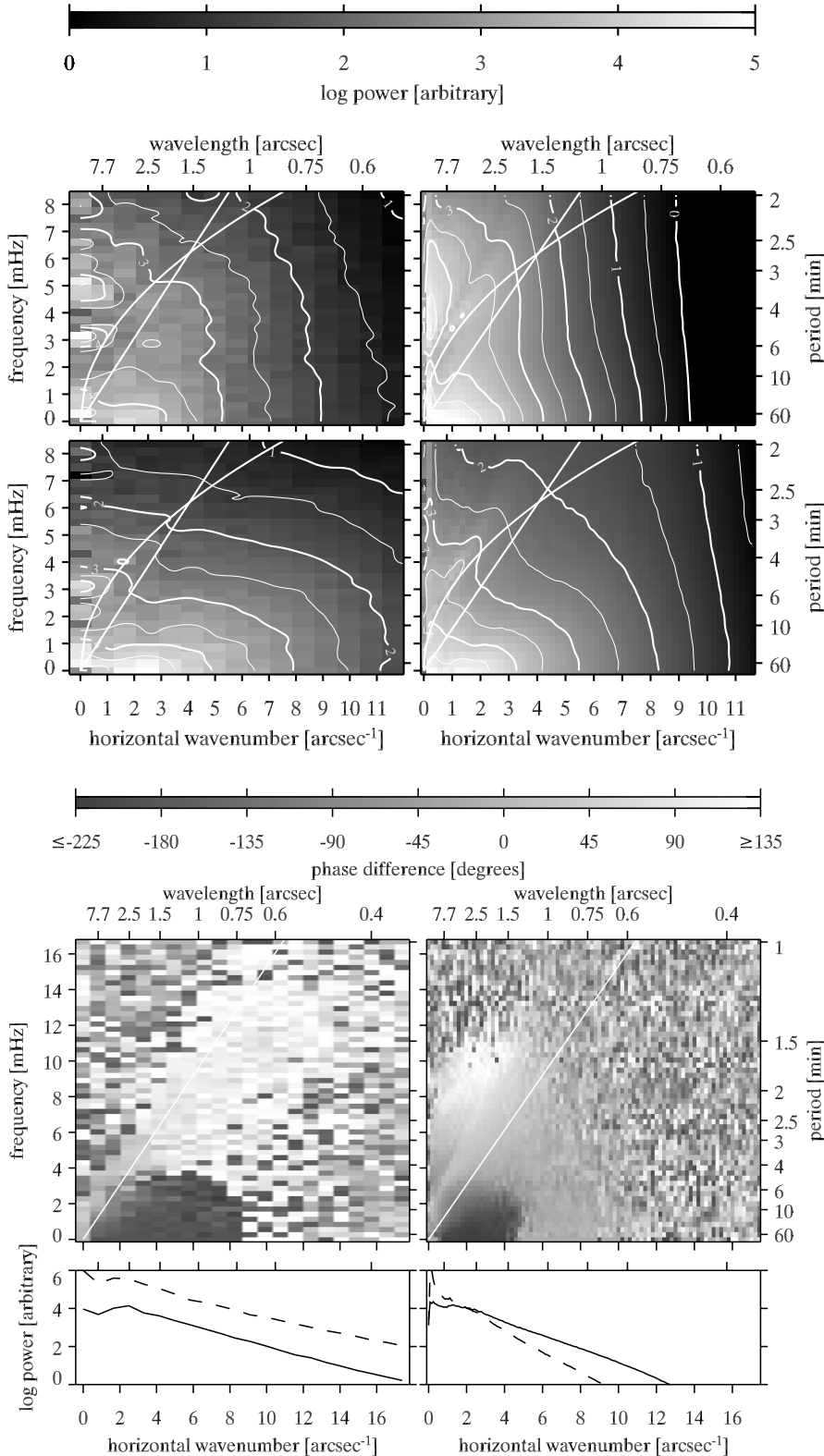
Fig. 5. Simulated (*left*) and observed (*right*) two-dimensional brightness power spectra. *Upper panels*: Ca II H. *Lower panels*: blue continuum (*left*) and G band (*right*). Axes: horizontal wavenumber k_h and temporal frequency f. The corresponding wavelengths and periods are specified along the top and at the right. Grey scale: logarithm of the brightness power after mean and trend removal and smoothing, as coded by the grey-scale bar above the figure and the contours. Slanted line: Lamb line $f = (1/2\pi)\, c_s\, k_h$ with $c_s = 7$ km s^{-1}. Curve: fundamental mode $f = (1/2\pi)\,\sqrt{g_{surf} k_h}$.

Fig. 6. *Upper panels*: two-dimensional phase differences in the format of Fig. 5 without contours and with larger axis extents. *Left*: simulated $\Delta\phi$ (Bc − Ca), right observed $\Delta\phi$ (Gb − Ca). Slanted line: Lamb line, $f = (1/2\pi)\, c_s\, k_h$ with $c_s = 7$ km s^{-1}. *Lower panels*: logarithm of the integrated brightness power in the 0–2 mHz frequency band. Solid: blue continuum (*left*) and G band (*right*). Dashed: Ca II H.

The low-frequency brightness power spectra (lower panels) are quite different[1]. The power spike at the lowest horizontal wavenumbers in the Ca II H observations is due to

magnetic network, not present in the simulation. The decrease of the brightness power with wavenumber differs between observation and simulation. We attribute the difference between the blue continuum and the G band slopes to a difference in spatial resolution. A test with simulated images that were smoothed to match the resolution of the December 2002 observations gave about the same slope. The difference between

---

[1] The power spectra in the lower-right panel of Fig. 6 differ slightly from the corresponding plot in Fig. 7 of Paper II because of correction of a minor programming error.

the observed and simulated Ca II H slope remained even with this smoothing. Indeed, inspection of the observed and simulated Ca II H images indicates larger small-scale contrast and sharpness in the latter. This may be due to the LTE and grey approximations for the radiative transfer in the simulation.

5. Discussion and conclusion

We have compared Dutch Open Telescope G-band and Ca II H observations with corresponding images obtained from non-magnetic radiation-hydrodynamics simulations with the CO^{5}BOLD code. We applied the same diagnostics as in Paper II to study the phenomenon of reversed granulation.

Overall, our results show good agreement between the observations and simulations. Figure 1 shows a high degree of similarity in the image samples. The contrast curves in Fig. 2 show good agreement for our choice of point spread function parameters, apart from the high contrast tail which is due to magnetic elements in the observations. The time-delay correlation curves of Fig. 3 also agree rather well; the fit of the time-delay autocorrelation curve for Ca II H in the upper panel is noticeably better when isolated magnetic elements are deleted from the sample. Also, the Fourier diagnostics in Figs. 4–6 show good overall correspondence, with the exceptions of the absence of a global p-mode signature in the simulated Fourier power and phase difference, and more brightness power at larger wavenumber in the synthetic Ca II H sequence.

We find an increase in anticorrelation between synthetic Ca II H and blue continuum images when smoothing to 1.5 arcsec resolution as in Paper II. Direct inspection of both the simulated and observed images smoothed to 1.5 arcsec still shows granulation and not a mesogranular pattern. Figure 1 shows observed and simulated blue continuum and Ca II H images at the time of maximum anticorrelation as shown in Fig. 3. Inspection of these images shows that not all dark intergranular lanes in the blue continuum images show up bright in Ca II H and, reversely, that not all bright features in Ca II H are located directly above intergranular lanes. Some of the bright features sit above the edge of a granule instead of a lane. We suggest that this incomplete mapping explains the partial nature of the anticorrelation and its increase with spatial smoothing.

In Paper II four explanations of reversed granulation were discussed: convection reversal, atmospheric gravity waves, acoustic waves, and intergranular magnetism. We claim that magnetic fields play at most a minor role since we obtain a satisfactory reproduction of the observed phenomenon with our purely hydrodynamic code, even though its treatment of radiative transfer is not perfect.

A preliminary analysis of simulation snapshots indicates that the Ca II H brightenings are in most cases caused by converging flows above an intergranular lane, which suggests that convection reversal is the principal mechanism (cf. Nordlund 1984b; Stein & Nordlund 1998). The roles of acoustic waves and gravity waves are not easily diagnosed, their evaluation needs further analysis of the simulation. Especially gravity waves are not easily recognized.

In summary, we claim that magnetic fields are of minor importance for the formation of reversed granulation. We suspect that convection reversal is the main cause of this phenomenon, and have started on a detailed analysis of our simulation to diagnose its physics.

References

Barklem, P. S., & O'Mara, B. J. 1998, MNRAS, 300, 863

Brandt, P. N., Rutten, R. J., Shine, R. A., & Trujillo Bueno, J. 1992, in Cool Stars, Stellar Systems, and the Sun, ed. M. S. Giampapa, & J. A. Bookbinder, Proc. Seventh Cambridge Workshop, Vol. 26: Astron. Soc. Pacific Conf. Ser., 161

Brandt, P. N., Rutten, R. J., Shine, R. A., & Trujillo Bueno, J. 1994, in Solar Surface Magnetism, ed. R. J. Rutten & C. J. Schrijver, NATO ASI Series C 433 (Dordrecht: Kluwer), 251

Deubner, F. L., & Mattig, W. 1975, A&A, 45, 167

Evans, J. W., & Catalano, C. P. 1972, Sol. Phys., 27, 299

Freytag, B., Steffen, M., & Dorch, B. 2002, Astron. Nachr., 323, 213

Gadun, A. S., & Sheminova, V. A. 1988, Inst. Theor. Phys. Kiev, preprint No. 88-87P

Hauschildt, P. H., Baron, E., & Allard, F. 1997, ApJ, 483, 390

Iglesias, C. A., Rogers, F. J., & Wilson, B. G. 1992, ApJ, 397, 717

Krijger, J. M., Rutten, R. J., Lites, B. W., et al. 2001, A&A, 379, 1052

Leibacher, J., Gouttebroze, P., & Stein, R. F. 1982, ApJ, 258, 393

Levy, M. 1971, A&A, 14, 15

Nordlund, Å. 1984a, in Small-Scale Dynamical Processes in Quiet Stellar Atmospheres, 174

Nordlund, Å. 1984b, in Small-Scale Dynamical Processes in Quiet Stellar Atmospheres, 181

Rutten, R. J., de Wijn, A. G., & Sütterlin, P. 2004a, A&A, 416, 333

Rutten, R. J., Hammerschlag, R. H., Bettonvil, F. C. M., Sütterlin, P., & de Wijn, A. G. 2004b, A&A, 413, 1183

Rutten, R. J., & Krijger, J. M. 2003, A&A, 407, 735

Schüssler, M., Shelyag, S., Berdyugina, S., Vögler, A., & Solanki, S. K. 2003, ApJ, 597, L173

Stein, R. F., & Nordlund, Å. 1998, ApJ, 499, 914

Stein, R. F., & Nordlund, Å. 2001, ApJ, 546, 585

Suemoto, Z., Hiei, E., & Nakagomi, Y. 1987, Sol. Phys., 112, 59

Suemoto, Z., Hiei, E., & Nakagomi, Y. 1990, Sol. Phys., 127, 11

Vögler, A. 2004, A&A, 421, 755

Wedemeyer, S. 2003, Ph.D. Thesis, University of Kiel, http://e-diss.uni-kiel.de/diss_764/

Wedemeyer, S., Freytag, B., Steffen, M., Ludwig, H.-G., & Holweger, H. 2004, A&A, 414, 1121